

# Monolayer Excitonic Semiconductors Integrated with Au Quasi-Periodic Nanoterrace Morphology on Fused Silica Substrates for Light-Emitting Devices

Yuheng Chen, Han Li, Mark Blei, Maoqi Cai, Haofeng Zang, Yonghua Lu, Sefaattin Tongay,\* and Ying Liu\*



Cite This: *ACS Appl. Nano Mater.* 2021, 4, 84–93



Read Online

ACCESS |



Metrics & More



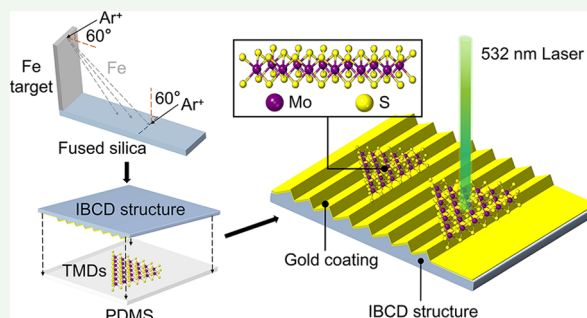
Article Recommendations



Supporting Information

**ABSTRACT:** Two-dimensional transition metal dichalcogenides (TMDs) have a promising future in the nanophotonics field due to their unique optoelectronic properties such as large exciton binding energies and carrier mobility. Among these properties, monolayer TMDs exhibit enhanced photoluminescence (PL) by utilizing micro-/nanostructure surface plasmon polariton (SPP) modes. In this work, we present a unique technique to achieve substantial PL enhancement by integrating MoS<sub>2</sub> monolayers to gold quasi-periodic nanoterrace morphology with gradient periods on fused silica substrates. Gold quasi-periodic nanostructures were fabricated through cost-effective and fast ion bombardment with iron co-deposition followed by a gold coating technique, and monolayers were deposited by a polymer-assisted technique. Our results show clear evidence that the light emission is enhanced due to the SPP modes produced by the quasi-periodic nanoterrace morphology. Comprehensive spectroscopy studies were performed on monolayer flakes with different laser polarizations, morphology periods, and temperatures to offer detailed insights on the mechanism behind PL enhancement. Together with numerical simulations, our results provided a basis for understanding the PL enhancement effects and shed light on future directions of high-efficiency light-emitting devices such as diodes, lasers, and heterostructure solar cells based on TMD monolayers.

**KEYWORDS:** 2D TMDs, photoluminescence enhancement, ion bombardment, quasi-periodic terrace morphology, plasmonics



## INTRODUCTION

Atomically thin 2D materials with strong spin-orbit interaction are attracting significant interest due to their novel optoelectronic,<sup>1,2</sup> electrochemical,<sup>3</sup> quantum,<sup>4,5</sup> electrical, and optical properties.<sup>6–9</sup> Among these 2D materials, transition metal dichalcogenides (TMDs) are an exciting class of materials that exhibit many interesting properties, including indirect to direct band gaps at monolayer limit,<sup>10</sup> large exciton binding energies,<sup>11</sup> and charge density waves<sup>12</sup> that arise from quantum confinement effects.<sup>13</sup> In these materials, transition-metal atoms are sandwiched by identical chalcogen atoms (S, Se, Te) at the top and bottom layers. It has been well established that a lack of inversion symmetry<sup>14–19</sup> in these crystals enable spin valley polarization effects and unlock new charge carrier degrees of freedom, which are believed to achieve optical readout and room temperature electrical modulation.<sup>20–30</sup> Additionally, these properties can be applied to many different applications such as transistors, solar and fuel cells, photocatalysis, and sensing technologies.<sup>31,32</sup>

Due to size confinement effects, TMDs exhibit enhanced photoluminescence (PL) and undergo indirect to direct band gap transitions in their single-layer limits.<sup>33</sup> However, chemical

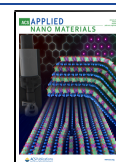
vapor deposition (CVD) produces unavoidable and deleterious defects responsible for low photoemission efficiency in many TMDs. High-efficiency light-emitting devices are paramount for current and future technologies that require ultralow threshold lasers,<sup>27</sup> light-emitting diodes (LEDs),<sup>34</sup> and photo-detectors.<sup>35–39</sup> To advance these optoelectronic fields, fundamental understanding of light-matter interactions in these materials is essential.

Nanophotonic cavities can manipulate optical fields at the nanoscale<sup>40–42</sup> and enhance the fluorescence of nano-emitters.<sup>43–45</sup> Besides dielectric cavities, which can enhance the electric field near-field with a distance of ~100 nm,<sup>46</sup> plasmonic cavities can penetrate several nanometers from the structured surfaces.<sup>47</sup> Utilizing surface plasmon polariton (SPP) modes is one of the most effective ways to improve

Received: September 2, 2020

Accepted: December 3, 2020

Published: December 16, 2020



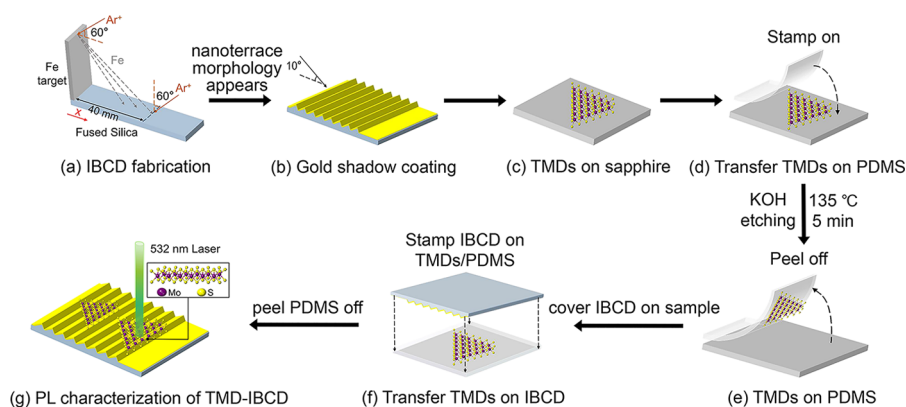


**Figure 1.** Process used for integrating TMD monolayers onto IBCD nanoterrace morphology. (a) Experimental geometry for ion bombardment with iron co-deposition. (b) Gold shadow coating on IBCD. (c) TMDs on sapphire. (d–f) TMDs transfer on IBCD by PDMS. (g) PL characterization of TMD-IBC D.

the PL performance of TMD monolayers.<sup>48–50</sup> The resonance frequency of surface plasmon strongly depends on the micro-/nanostructure characteristics such as composition, shape, and structure size.<sup>51–54</sup> Precious metal plasmonic nanostructure templates, as an effective method to improve the PL performance of 2D materials, have received much attention in recent years.<sup>55,56</sup> However, previous methods to produce plasmonic nanostructure templates for increasing the PL intensity use relatively high-cost electron beam lithography equipment or lithographic approaches.<sup>57</sup> Therefore, finding a simple and efficient plasmonic nanostructure template to couple with TMD monolayers has become an emerging research field.

Low-energy ion bombardment (IB) is a very promising nanofabrication tool with the potential to generate large area nanostructures in a single process. It can induce diverse nanostructures on various materials, and is a cost-effective and maskless bottom-up process. Nanotemplates produced by direct IB are being increasingly applied in optical devices,<sup>58–61</sup> optoelectronic devices,<sup>62</sup> and magnetic modulation.<sup>63</sup> IB with impurity co-deposition (IBCD)<sup>64–67</sup> or surfactant sputtering<sup>68</sup> offers the potential to tailor various nanopatterns with enhanced dimensions in a deterministic way. Impurities play an important role in the surface morphology of the nanoterrace produced by IBCD (simplified as the IBCD structure in the following). This allows for structures with gradient periods produced in a single-step fabrication process, in particular, promoting the terraced growth of nanostructures and adjusting pattern symmetry.<sup>69,70</sup> Based on the quasi-periodic nanoterrace morphology produced by IBCD as a template, it demonstrates a promising option for the plasmonic enhancement of light emission for 2D TMD applications.

In this work, to expand the future applications of high-efficiency light-emitting devices, we first utilized the IBCD structure to fabricate plasmonic resonators. Through adjusting the structural characteristic of the IBCD structure, we tuned SPP modes and realized the enhancement and manipulation of the light emission from TMD monolayers. Compared to the plasma antenna structures processed by conventional nanofabrication methods,<sup>49,50</sup> IBCD offers a number of advantages including cost-effective approach and fast processing. After coupling the TMD monolayers to gold-coated IBCD structures with a conventional polymer transfer process (TMD-IBC D), we can flexibly tune the PL enhancement by simply varying the period of the IBCD-induced nanoterrace morphology (the

IBC D period for brevity in the following). We observed great enhancement in light emission from the TMD-IBC D device, which directly correlated with the IBC D periods. Furthermore, laser polarization, single monolayer mapping, and low temperature PL measurement were performed to show that the PL enhancement is dramatically influenced by the IBC D structure directionality, strains that originate from the structure periodicity and temperature variation.

## RESULTS AND DISCUSSION

The process used for integrating TMD monolayers onto IBCD nanoterrace morphology is demonstrated in Figure 1. The quasi-periodic nanoterrace morphology was fabricated on fused silica substrates via IBCD (Figure 1a). In contrast to structures fabricated with conventional IB, the nanoterraced IBCD structures used in this work have a gradient change in period and height along the  $x$  axis across the fused silica surface, and the profile shape is very similar to that of a blazed grating, allowing for the period and height to be tuned to outline the structure shape features. Figure 2a–c shows the atomic force microscopy (AFM) topographs at distances from the iron target of 10, 20, and 30 mm, respectively. The rulers represent the typical period in each topograph. Figure 2a'–c' shows typical cross-section profiles corresponding to Figure 2a–c, respectively. Figure 2d demonstrates the gradation trend of the IBCD structure's representative period and height estimated from AFM topographs. These figures show that as the distance to the iron target increases, the period and height of IBCD also increases. The sample is then sputter coated (incident angle is  $80^\circ$  from the the normal) with 10 nm 99.99% gold (Figure 1b). The AFM topographs at distances from the iron target of 10, 20, and 30 mm after 10 nm gold coating are shown in Figure S1. The roughness ( $R_a$ ) of the IBCD morphology of each position before and after gold coating is also provided. The positive-sloped facets of the nanostructure were faced to the gold target and preferentially coated with thicker gold than the negative facets, whose thickness of gold coating is approximately 3 nm. We believe that this can be attributed to the divergence of the ion beam during gold coating, and asymmetric gold thickness plays a key role in the formation of plasma resonance mode. In the following discussion, the IBCD gold coating thickness will be simplified as 10 nm, which is the thickness on positive-sloped facets. So far, we fabricated the plasmonic nanostructure to

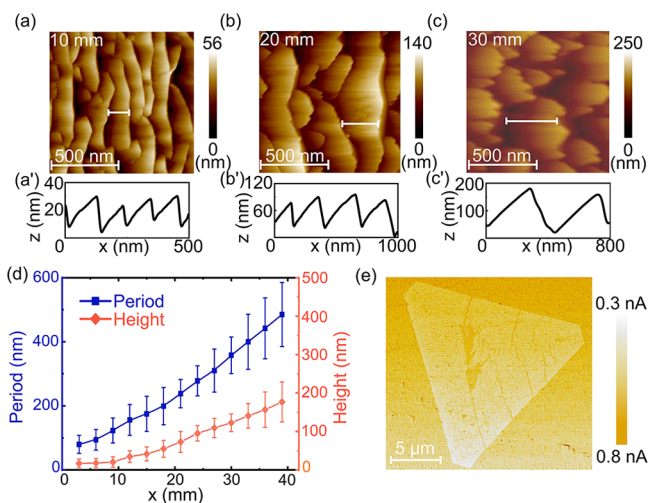


**Figure 2.** (a–c) AFM topographs at distances from the iron target of 10, 20, and 30 mm of the IBCD structure sample. Area shown by each topograph is  $1 \times 1 \mu\text{m}^2$ . The rulers represent the representative period in each topograph. (a'–c') Typical section profiles of panels (a–c). The ranges of them are 500, 1000, and 800 nm. (d) Representative period and height from AFM topographs. (e) Lateral force mode AFM topograph of the MoS<sub>2</sub> monolayer on the surface of the IBCD structure. The area shown by the topograph is  $20 \times 20 \mu\text{m}^2$ .

bring about SPP modes, which can enhance the PL intensity of the TMD monolayers.

MoS<sub>2</sub> monolayers are transferred by the polymer-assisted method aligned on the surface of the IBCD structure.<sup>71</sup> Figure 2e shows the AFM image at lateral force mode of the MoS<sub>2</sub>

monolayer on IBCD. The contrast between the IBCD structure and the MoS<sub>2</sub> monolayer is presented by the current due to the difference of friction between diverse surfaces. The MoS<sub>2</sub> monolayers side lengths are approximately 10–15  $\mu\text{m}$ , making them large enough to cover more than 20 of the IBCD fabricated maximum 500 nm periods.

To ensure the consistency of the MoS<sub>2</sub> monolayers in PL measurement, all transferred MoS<sub>2</sub> monolayers were selected from the same growth process. Furthermore, to enable direct comparison of PL intensity from different structure periodicity regions, it is necessary to discuss the polarized PL intensity distribution and the PL intensity consistency of MoS<sub>2</sub> monolayers at the same transfer region. The PL intensity curves plotted in Figure 3a show the MoS<sub>2</sub> monolayers' light emission on gold IBCD structures for the IBCD main axes orthogonal and parallel to the laser polarization (laser TM mode and TE mode) and on the non-IBCD region, respectively. The MoS<sub>2</sub> monolayers on IBCD show a striking anisotropic behavior as the angle between the polarization direction and the IBCD main axis,  $\theta$ , varies from 0 to 90° by changing the in-plane orientation of the sample mounted on a rotating stage. The PL intensity is strongly amplified for laser polarized along the IBCD main axis. It also shows that when the laser polarization is parallel to the IBCD main axis, the PL intensity is still greater than the non-IBCD case. This phenomenon is due to the quasi-periodic feature and discontinuity of the IBCD structure. As shown in Figure 2, a small part of the IBCD structure has structural components perpendicular to the main axis, although their ratio is much lower than the parallel component. This part of the nanostructure brings a small amount of SPP enhancement

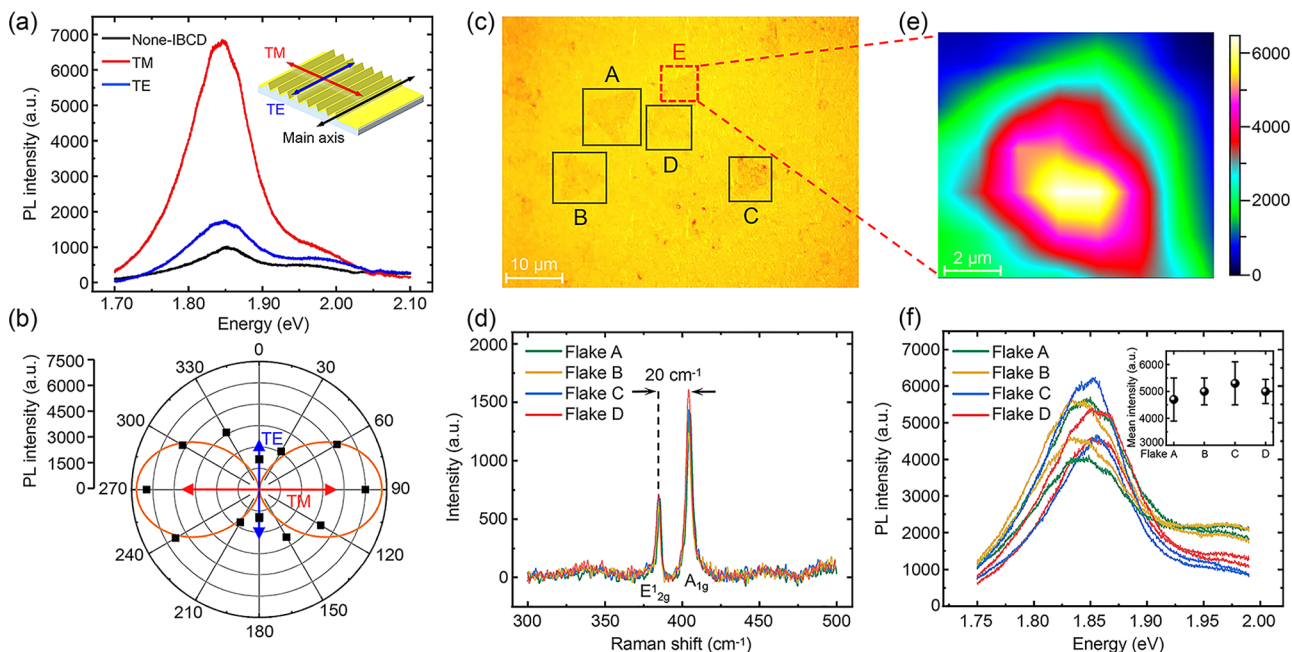


**Figure 3.** (a) Polarized PL intensity curves of the MoS<sub>2</sub> monolayers on gold IBCD structures and unpolarized PL intensity curve of the MoS<sub>2</sub> monolayer on the non-IBCD region. Laser transverse-magnetic (TM) and transverse-electric (TE) modes correspond to the polarization directions perpendicular and parallel to the IBCD structure main axis, respectively (see insets). (b) Polar plots of the PL intensity as a function of  $\theta$ , i.e., the angle between the laser polarization and the IBCD main axis. The orange trace is proportional to the  $\sim \sin^2(\theta)$  function. (c) Image of the MoS<sub>2</sub> flakes transferred onto IBCD with a 320 nm period obtained by optical microscopy with a 20 $\times$  magnification. (d) Raman spectra of flakes A–D. (e) Mapping result of flake E from panel (c), showing the PL intensity distribution of a single MoS<sub>2</sub> monolayer flake. The color scale indicates the PL intensity in arbitrary units. (f) PL spectra of flakes A–D measured at the center region of each MoS<sub>2</sub> monolayer. The inset shows the mean intensity, taking into account the statistical error of the four flakes measured.

effect as shown in the Figure 3a TE mode PL intensity curve. The signals (black squares) in Figure 3b appear with two-lobe behavior orthogonal to the IBCD main axis ( $\theta$  is 90 and 270°) and with an angular distribution qualitatively described by a  $\sim \sin^2\theta$  trigonometric law (orange curves).<sup>72</sup> The above experimental results can be rationalized in terms of the variation in resonance intensity of SPP modes due to the anisotropic IBCD morphology and also can be confirmed in the simulated electric field intensity near-field distribution results in Figure 6.

Figure 3c shows the optical image of the MoS<sub>2</sub> flakes transferred onto the IBCD with 320 nm periodicity. Different triangular monolayer flakes (A–E) are identified.<sup>73</sup> These flakes were analyzed by Raman and PL spectra. Figure 3d shows the Raman spectra of different selected flakes (A–D); they are almost consistent and overlapped. The two main peaks are located at 385 and 405 cm<sup>-1</sup>, which belong to the main phonon vibrations E<sub>2g</sub><sup>1</sup> and A<sub>1g</sub>, respectively.<sup>74</sup> The 20 cm<sup>-1</sup> wavenumber difference between these two peaks confirms the monolayer characteristic of the MoS<sub>2</sub> flakes.<sup>75</sup> The PL intensity is another indicator for a monolayer characteristic.<sup>76</sup> In order to analyze the PL intensity distribution in a single flake, we carried out a PL mapping in flake E (Figure 3e). The intensity in the center region of the monolayer is basically constant and higher than the PL intensity of the periphery. To ensure the PL stability of different flakes within the same periodicity region, PL intensity curves obtained in the central region of the selected flakes (A–D) are shown in Figure 3f, and all curves showed similar peak energy  $\sim 1.85$  eV, indicating the 2D MoS<sub>2</sub> characteristic. The inset shows that the PL intensity barely changes within the same periodicity region, confirming the similar quality of the flakes. Therefore, in the following PL intensity measurement, we utilized the laser polarization perpendicular to the IBCD main axis (TM mode) and measure the central region of the MoS<sub>2</sub> monolayer flakes to ensure the reliability of PL intensity measurement.

According to the previous AFM measurement result, the surface of the MoS<sub>2</sub> monolayers was transferred on the top of the IBCD structure and formed a plateau within the material region. Due to the nature of the IBCD structure as well as the weight of the transferred monolayer, the contacts of the IBCD structure and MoS<sub>2</sub> only happen at the IBCD structure's peaks, while MoS<sub>2</sub> sinks into the valleys between the peaks of the structure. To understand how the IBCD structure and the MoS<sub>2</sub> monolayers interact, we performed PL mapping measurement with a scan step of 0.1  $\mu\text{m}$ . As shown in Figure 4a, the PL intensity of the MoS<sub>2</sub> monolayer is characterized under a 100 $\times$  objective lens, and the red square represents the mapping range  $1 \times 1 \mu\text{m}^2$ . The inset in Figure 4a shows the IBCD structure profile beneath the MoS<sub>2</sub> monolayer with a period of approximately 200 nm, and Figure 4b shows a representative PL spectra of MoS<sub>2</sub>, highlighting the curve peak position and intensity integral (from 1.75–1.93 eV energy range), which is the basis for the following results. Figure 4c shows the PL intensity mapping result, where the yellow and blue regions represent higher and lower PL intensities, respectively. The period observed in the PL mapping directly correlates to the IBCD nanostructure period. Taking a closer look, the yellow region is narrower than blue region in width. Furthermore, the gaps between the yellow regions are approximately 190–215 nm, which is in excellent agreement with the IBCD structure period of 200 nm. To show the broad

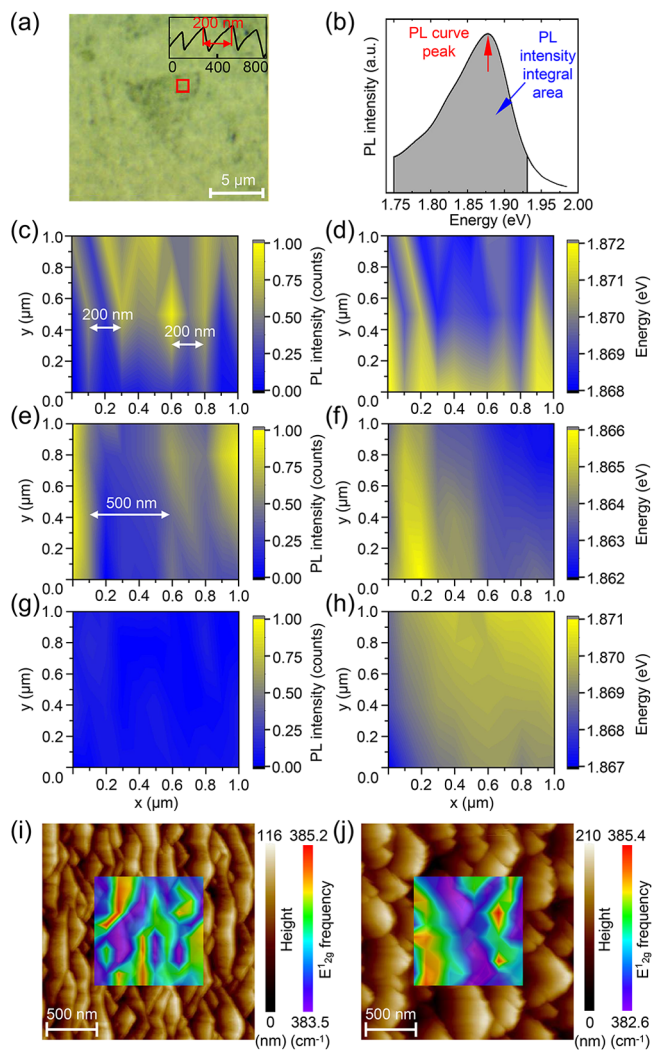


**Figure 4.** (a) MoS<sub>2</sub> monolayer on the optical characterization platform under a 100 $\times$  objective lens, and the red square is the mapping range which is  $1 \times 1 \mu\text{m}^2$ . The inset profile shows the IBCD structure profile beneath the MoS<sub>2</sub> monolayer. (b) Schematic illustration of the PL curve peak position and PL intensity integral area. (c, e, g) PL intensity mapping results in 200 and 500 nm periodicity and non-IBCD regions. The range of images is  $1 \times 1 \mu\text{m}^2$ . (d, f, h) Energy of the PL intensity curve peak mapping results in 200 and 500 nm periodicity and non-IBCD regions. The range of images is  $1 \times 1 \mu\text{m}^2$ . (i, j) Raman mapping ( $1 \times 1 \mu\text{m}^2$ ) of the E<sub>2g</sub> mode for the monolayer MoS<sub>2</sub> on IBCD with periods of 200 and 500 nm, respectively. The Raman maps are superimposed on each AFM topograph ( $2 \times 2 \mu\text{m}^2$ ).

applicability of this technique, we repeated the PL mapping measurement previously described using the IBCD structure with a 500 nm period (Figure 4e), and it is observed that this technique can be applied to a wide period range of the IBCD structure.

To better understand how the enhancement effect varies within one monolayer, a closer look was taken to determine the relationship of blue or yellow mapping regions and the structure geometry. Based on the previous literature, it is known that the band gap of MoS<sub>2</sub> will redshift under tensile strain,<sup>77</sup> indicating that the higher PL peak center is representative of a lower strain; in other words, the material that contacts with the top part of the IBCD structure will have a greater strain and lower band gap; while the material that

freely sinks in the valley of IBCD structure will have a lower strain as well as a larger band gap. In Figure 4f, the yellow region, which represents a higher energy and lower strain region, exists from 0.1 to 0.6  $\mu\text{m}$  in the longitudinal direction, indicating that the valley of the IBCD structure is located in between. Combining the plot in Figure 4d, we can confidently conclude that the valley of the IBCD structure produces a lower PL intensity and thus a lower PL enhancement effect, and the period of enhancement effects matches well with the period of the IBCD structure. Our results are repeatable on different samples as well as different periods. As a reference, MoS<sub>2</sub> monolayers were also transferred to flat fused silica substrates and were studied. Figure 4g,h shows that the PL intensity and band gap are uniform while supported on flat fused silica substrates.

Compared with PL spectra, Raman spectra more significantly depends on the local strain of TMDs. The physical source of the Raman frequency offset of the E<sub>2g</sub><sup>1</sup> mode of TMDs is usually closely related to the strain of the monolayer flake induced by underlying nanostructured templates.<sup>78–80</sup> In this study, the Raman frequency offset indicates the local strain of the monolayer MoS<sub>2</sub> flake induced by the IBCD structure.

Raman mapping results (1 × 1  $\mu\text{m}^2$ ) of the frequency positions of E<sub>2g</sub><sup>1</sup> modes are shown in Figure 4i–j. The maps are superimposed on the AFM topographs (2 × 2  $\mu\text{m}^2$ ) of the corresponding IBCD 200 and 500 nm periodicity regions, respectively. Similar to the PL maps, both Raman maps show strong anisotropy and reproduce the actual morphological characteristics of the IBCD structure even better than PL maps. This indicates that the Raman peaks of the monolayer along a specific nanoterrace ridge or valley are approximately same. A large frequency shift, i.e., the Raman peak shift is observed perpendicular to the direction of the IBCD main axis, especially those between the peaks and valleys of the IBCD structure. The spatial distribution of the frequency offset depends on that of the morphology of the IBCD. The nanosheets at the top of the peak are subjected to greater strain and lead to the redshift of E<sub>2g</sub><sup>1</sup> mode frequency as in the references.<sup>78–80</sup> As the peak spacing increases from 200 to 500 nm, the strain increased, which corresponds to the redshift of Raman peak from 1.7 and 2.8 cm<sup>-1</sup>, respectively.

Above, we demonstrated how the separate IBCD period impacts the PL intensity of MoS<sub>2</sub> monolayers. However, as mentioned earlier, the period of the IBCD structure increases across its surface. This allowed for the observation of how gradient periods of the IBCD affects PL enhancement. Using a similar setup as previously discussed, the MoS<sub>2</sub> monolayers were transferred onto the IBCD structure with 80, 140, 320, 410, and 480 nm periods and onto a non-IBCD region as a reference. The MoS<sub>2</sub> monolayers images from the optical characterization platform under a 20× objective lens are shown in Figure S2. As shown in Figure 5a, PL spectra of MoS<sub>2</sub> transferred onto different periodicity regions are compared, and various positions were measured at the same respective period before being averaged and compared in Figure 5d. In Figure 5a, the PL intensity drops monotonically from the smallest to the largest periodicity regions but is still stronger than that of MoS<sub>2</sub> on a non-IBCD region. The PL intensity at the 80 nm periodicity region is enhanced by approximately seven-fold compared with the non-IBCD region. This phenomenon shows that the PL intensity is very sensitive to the period of the IBCD structure, and the coupling between MoS<sub>2</sub> monolayers and the IBCD structure plays a significant

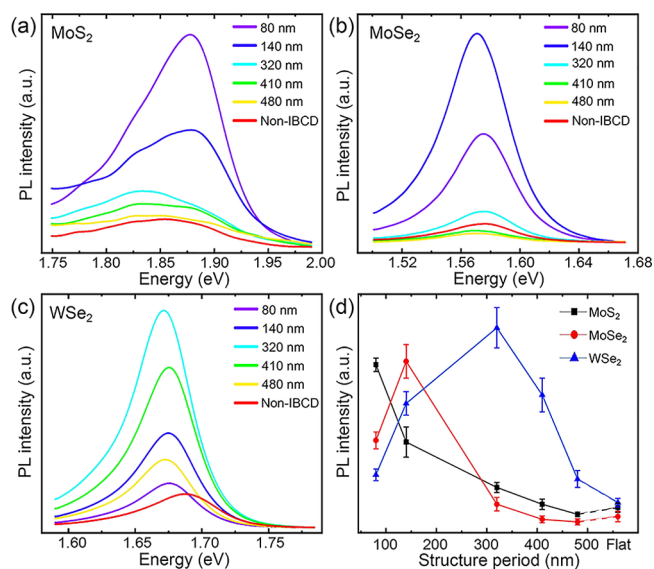


**Figure 5.** (a–c) PL average intensity curves in 80, 140, 320, 410, and 480 nm periodicity regions and non-IBCD regions of MoS<sub>2</sub>, MoSe<sub>2</sub>, and WSe<sub>2</sub>. (d) Summary curves of PL intensity at each region of three TMD-IBCD devices. Dashed lines link to the non-IBCD region PL intensity.

role in the amplification of the PL intensity. To show the broad applicability of this novel approach, other TMD monolayers (Figure 5b,c), MoSe<sub>2</sub> and WSe<sub>2</sub> monolayers were also transferred onto the five IBCD fabricated structure regions and one flat, non-IBCD substrate. Figure 5d shows that the PL intensity peak of MoSe<sub>2</sub> appears at the 140 nm periodicity region, which is about 13-fold stronger than that of the non-IBCD region, while the intensity peak of WSe<sub>2</sub> appears at the 320 nm periodicity region, which is about eight-fold stronger than that of the non-IBCD region.

To explore the principles governing the PL enhancement of MoS<sub>2</sub>-coupled IBCD devices, we simulated the near-field distribution originating from the SPP modes from the underlying IBCD structure (Figure 6a). We used the finite-difference time-domain (FDTD) method for numerical simulations,<sup>81–83</sup> and the near-field distribution simulation performed was carried out using 10 nm-thickness gold coating ideal blazed grating lines as a simplified IBCD structure with a period of 80 nm and an incident laser wavelength of 680 nm (the wavelength corresponding to the MoS<sub>2</sub> monolayer's PL curve peak at room temperature). Representative structure parameters such as period, height, and blazed angle are from AFM topographs. For transverse magnetic (TM) wave guide modes, the amplitude of the electric field decays exponentially away from the surface of the gold film and maximizes at the tips of IBCD structure, indicating the excitation of SPP resonance modes. For transverse electric (TE) wave guide modes, the electric field intensity distribution does not change with the structure profile. We chose the TM modes transmittance instead of TE modes to characterize the resonance wavelength of the SPP modes since it is necessary that the electric field is bounded at the surface of gold film and propagates along the surface.<sup>84,85</sup>

The TM polarization transmittance of the 10 nm-thickness gold coating IBCD structure with periods of 80, 140, and 320 nm was simulated using 250–900 nm incident wavelengths by the FDTD method. Since IBCD structures with a period larger

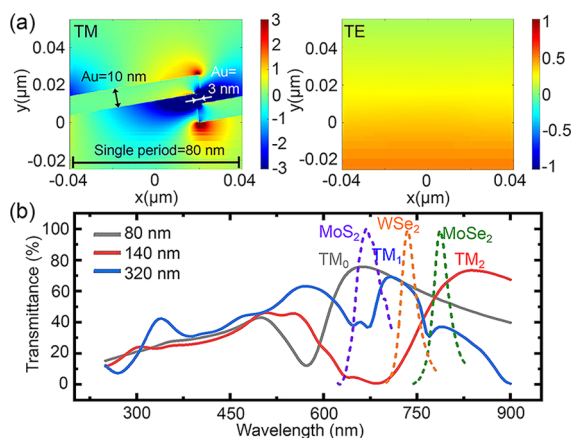


**Figure 6.** (a) Near-field distribution (Left-TM  $\text{Re}\{E_y\}$ , Right-TE  $\text{Re}\{E_z\}$ ) produced by ideal grating lines similar to the IBCD structure at the 680 nm wavelength with an 80 nm period (indicated by the ruler) and 10 nm gold thickness. (b) Transmittance curves simulation (gray, 80 nm; red, 140 nm; blue, 320 nm) in the 250–900 nm incident light wavelength range. The purple (orange/green) dashed line represents the PL spectrum of the MoS<sub>2</sub> (WSe<sub>2</sub>/MoSe<sub>2</sub>) monolayers overlapping the resonance peak at room temperature. TM<sub>0</sub>, TM<sub>1</sub>, and TM<sub>2</sub> indicate the peaks of gray, blue, and red curves, respectively.

than 350 nm break seriously in the vertical direction and it cannot be simulated with ideal grating lines (Figure 2c), we only simulate the structure whose period is below 350 nm. Figure 6b shows that the three transmittance curves (gray, 80 nm; red, 140 nm; blue, 320 nm) have peaks at different positions from 600–850 nm in the spectrum, which are marked as TM<sub>0</sub>, TM<sub>2</sub>, and TM<sub>1</sub>. The purple (orange/green) dashed line represents the PL spectrum of the MoS<sub>2</sub> (WSe<sub>2</sub>/MoSe<sub>2</sub>) monolayers overlapping the resonance peak at room temperature. According to Figure 6b, the excitation wavelength of the MoS<sub>2</sub> PL curve is relatively close to TM<sub>0</sub>, that is, the 80 nm periodicity region will produce stronger SPP modes when MoS<sub>2</sub> is excited than the other two period structures. Therefore, it is inferred that when the MoS<sub>2</sub> monolayers are transferred to the 80 nm periodicity region, the PL intensity will have the most obvious enhancement effect. Similarly, transferring WSe<sub>2</sub> to the 320 nm periodicity region and MoSe<sub>2</sub> to the 140 nm periodicity region will produce a stronger PL enhancement effect than other regions. The results of the numerical simulation agree very well with the aforementioned experimental results and also reflect the significant influence of SPP modes on the regulation of the TMD monolayers' PL intensity. We provided the measured transmittance curves of IBCD nanostructures at 80, 140, and 320 nm periodicity regions after 10 nm gold coating in Figure S3 for comparison. Compared with the transmittance simulation results obtained by the FDTD method, the main variations of the measured transmittance curves are as follows: (1) the transmittance peak value is decreased; (2) the resonance peak width is broadened; and (3) the gold absorption peak at ~500 nm and the resonance peak are merged. Note that the broadening of plasmonic spectra is intrinsic for self-organized nanostructures. This has been experimentally observed<sup>86,87</sup> and theoretically reproduced.<sup>88,89</sup> To clearly show that the resonance wavelength changes at different periodicity regions of IBCD and their coupling relationship with the peak of the TMDs, we used the FDTD simulation results of ideal grating lines here.

Previously, we applied large incident angle gold coating on the surface of the IBCD structure, and it was transformed into plasmonic resonator because of SPP modes. Plasmonic nanostructures are especially effective for enhancing light–matter coupling in TMD monolayers because the electromagnetic field can be strongly localized and enhanced in the near field region of the plasmonic nanostructure. The electric field within our resonator formed by the IBCD structure has a strong TM mode component, ensuring intensive interaction with exciton resonances in TMD monolayers. The effective TMD-IBCD coupling is enhanced, and PL intensity enhancement of up to 13 times is produced within different TMD monolayers. In addition, it is also possible to manipulate the degree of enhancement of the PL intensity at different structure periodicity regions from Figure 5.

In order to understand the temperature-dependent excitonic behavior of MoS<sub>2</sub> when coupled to the IBCD structure, we conducted low temperature PL measurements on two MoS<sub>2</sub> samples from 10 to 300 K that were transferred onto the 80 nm periodicity region in which enhancement is strongest, and a flat fused silica substrate, which was not subjected to any ion bombardment process. In Figure 7a, the solid lines and dashed

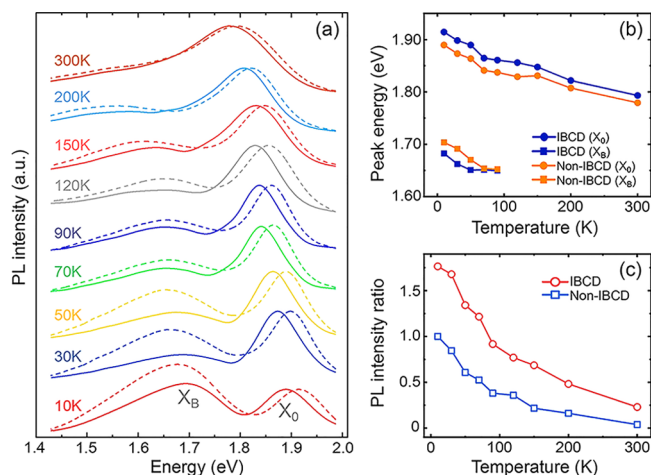


**Figure 7.** (a) PL spectrum from MoS<sub>2</sub> PL intensity measurement in the temperature range of 10 to 300 K, corresponding to the MoS<sub>2</sub> on the 80 nm periodicity region (dashed lines) and MoS<sub>2</sub> on the non-IBCD region (solid lines). (b) Center wavelengths of the X<sub>0</sub> peak (IBCD region, blue circle; non-IBCD region, orange circle) and the X<sub>B</sub> peak (IBCD region, blue square; non-IBCD region, orange square) as a function of temperature from 10 to 300 K. (c) PL intensity ratio as a function of temperature corresponding to the MoS<sub>2</sub> on IBCD (red) and MoS<sub>2</sub> on the non-IBCD region (blue).

lines represent the recorded PL spectra of MoS<sub>2</sub> transferred onto the non-IBCD fused silica substrate and the 80 nm periodicity region, respectively. As the temperature decreases, the PL blueshifts and the FWHM narrows, and a new peak appeared. To distinguish the new emerging peak from the A exciton peak, we labeled them X<sub>B</sub> and X<sub>0</sub>, respectively. The X<sub>B</sub> peak is broader than the X<sub>0</sub> peak and is thermally quenched for temperatures above 90 K. For the IBCD and non-IBCD regions, the center wavelengths of the X<sub>0</sub> peak and X<sub>B</sub> peak are plotted as a function of temperature in Figure 7b. For MoS<sub>2</sub> monolayers on the non-IBCD region, the X<sub>0</sub> peak of the PL spectrum will produce a stronger redshift at higher temperatures. The X<sub>B</sub> peak will also be redshifted until it disappears at 90 K. At all temperatures, the X<sub>0</sub> peak of the PL spectrum on

IBCD region has a systematic blueshift relative to the  $X_0$  peak on non-IBCD region. At temperatures below 150 K, the displacement is about 0.02–0.03 eV. The degree of blueshift decreases with increasing temperature and basically vanishes above 150 K. However, the  $X_B$  peak of the IBCD region has a certain redshift relative to the  $X_B$  peak of the non-IBCD region. When temperature increases, bound excitons can be thermally activated into the delocalized states and captured by the competing nonradiative decay channels or recombine as free excitons. Therefore, it can be expected that the intensity of localized exciton emission will decrease monotonically with increasing temperature, while the intensity of free exciton emission will increase, which is exactly what we observed for the ones labeled as  $X_B$  and  $X_0$ . The weakly localized carriers are first thermally activated to the delocalized state, so when the temperature rises from a low temperature, the peak positions will show a redshift. In addition, except the direct strain effect on the exciton energy, localized excitons are also affected by strain-induced defect changes. It should be noted that the  $\text{MoS}_2$  monolayer has a positive thermal expansion coefficient ranging from  $8 \times 10^{-6} \text{ K}^{-1}$  at 300 K to less than  $1 \times 10^{-6} \text{ K}^{-1}$  at 10 K.<sup>90,91</sup> The IBCD structure (fused silica) has a relatively small thermal expansion coefficient of  $0.55 \times 10^{-6} \text{ K}^{-1}$  at 300 K. The mismatch of thermal coefficients results in a uniaxial tensile strain inside  $\text{MoS}_2$  as the temperature varies. The different shapes of the fused silica profile in the IBCD and non-IBCD regions exacerbate the strain variation at low temperatures. The difference between the peak displacements of localized excitons and the free excitons in the IBCD/non-IBCD region shows that the strain-induced defect changes dominate the localized exciton peak displacement. As shown in Figure 7c, the relationship between the PL intensity of the IBCD and non-IBCD regions as a function of temperature is plotted. We set the intensity of the non-IBCD region on 10 K as 1 to show the ratio of PL intensity. When the temperature increases, the PL intensities of both the IBCD and non-IBCD regions decrease. Also, at each temperature, the PL intensity of the IBCD region is greater than that of the non-IBCD region. However, as the temperature increases, the difference between them gradually narrows. Also, until 300 K, it reaches the room temperature measurement state as described above, and the IBCD region has a seven-fold enhancement in PL intensity relative to the non-IBCD region. Therefore, even if the PL intensity of  $\text{MoS}_2$  monolayers increases naturally at low temperature conditions, the SPP modes can still ensure that the PL intensity of IBCD regions is significantly higher than that in non-IBCD regions, which proves the stability of plasmonic enhancement in temperature variation.

## CONCLUSIONS

In summary, we demonstrated the enhancement and manipulation of light emission from  $\text{MoS}_2$  monolayers integrated on the ion bombardment with iron co-deposition (IBCD)-induced quasi-periodic nanoterrace morphology. Combined with gold shadow coating, the IBCD structure exhibits remarkable features of rapid fabrication, simple process, and structural characteristic diversification, generating significant SPP modes for  $\text{MoS}_2$  monolayers and even other TMD monolayers ( $\text{MoSe}_2$ ,  $\text{WSe}_2$ ) on a single device. Compared with other PL enhancement methods,<sup>40,48–50</sup> the gradient periods of IBCD in our work not only bring about efficient light emission but also directly correlates with tunable enhancement performance. In addition, comprehensive spec-

troscopy studies on laser polarizations and intensity variations within single TMD monolayers and under low temperatures down to 10 K also offer detailed insights on the mechanism behind PL enhancement. Our work therefore develops common understanding of SPP mode-induced light emission from excitonic semiconductors and paves the way for chip-integrated light-emitting devices for application in enhanced light–matter interaction and photodetection.

## EXPERIMENTAL SECTION

**Fabrication of Gold Quasi-Periodic Nanoterrace Morphology (IBCD Structure).** First, the end of a  $60 \times 20 \times 2 \text{ mm}^3$  fused silica ( $\text{SiO}_2$ ) sample was attached to an iron target (purity: 99.9%,  $30 \times 20 \times 0.5 \text{ mm}^3$ ) and placed in the IB chamber. The iron target and  $\text{SiO}_2$  sample were bombarded with  $\text{Ar}^+$  ions for 30 min.<sup>70</sup> After bombardment, the structure region of  $40 \times 20 \text{ mm}^2$  was created on the sample. Next, the sample was placed in an ion beam coating machine and deposited with 10 nm 99.99% purity gold. The base pressure was approximately  $1.5 \times 10^{-3} \text{ Pa}$ , and the coating rate was 4.4 nm/min. The incident angle of the ion beam was  $80^\circ$  from the normal to the sample.

**Synthesis of TMD Monolayers.**  $\text{MoS}_2$  monolayers are grown with chemical vapor deposition (CVD) in a single-zone Lindberg tube furnace. A total of 3 mg  $\text{MoO}_3$  is placed in an alumina boat and mixed with 0.5 mg NaCl. A 285 nm  $\text{SiO}_2/\text{Si}$  substrate is placed on top of the alumina boat, and S is placed 16 cm upstream from the alumina boat. A 20 sccm  $\text{N}_2$  serves as the carrier gas. The furnace is heated up to  $580^\circ \text{C}$  in 15 min and kept at  $580^\circ \text{C}$  for 10 min before natural cooling.

$\text{MoSe}_2$  monolayers are grown in the same setup with  $\text{MoO}_3$  and S as precursors. A total of 3 mg  $\text{MoO}_3$  is placed in alumina boat with 285 nm  $\text{SiO}_2/\text{Si}$  substrate on top. Se is placed 18 cm upstream in an alumina crucible. A 20 sccm  $\text{N}_2$  is used as the carrier gas. The furnace is heated up to  $680^\circ \text{C}$  in 18 min and kept at  $680^\circ \text{C}$  for 10 min before natural cooling.

$\text{WSe}_2$  monolayers are grown using  $\text{WO}_3$  and Se as precursors. A total of 60 mg  $\text{WO}_3$  is placed in an alumina boat, and 1.5 g Se is placed 18 cm upstream in an alumina crucible. Polished sapphire substrates are placed directly on top of a  $\text{WO}_3$  precursor. An 80 sccm carrier gas ( $\text{Ar}:\text{H}_2 = 9:1$ ) is used to flush the system before heating for 15 min to eliminate air. The furnace is heated up to  $850^\circ \text{C}$  in 17 min and kept at  $850^\circ \text{C}$  for 20 min before natural cooling.

**Monolayers Transfer onto the IBCD Structure.** As-grown TMD monolayers are transferred onto the IBCD structure with the polymer-assisted transfer method. Polydimethylsiloxane (PDMS) is covered on the TMD sample and then together etched in a 2 mol/L potassium hydroxide (KOH) solution at  $130^\circ \text{C}$  for 2 min. Then, the PDMS layer was lifted off from the substrate and washed in distilled water. Then, the dried PMDS was attached on the IBCD structure with help of the transfer stage to realize point to point transfer.<sup>71</sup>

**Spectroscopy Measurements.** Photoluminescence (PL) of TMD-IBCD samples were performed with a homemade system in backscattering configuration. A 532 nm laser with a polarization perpendicular to the IBCD main axis was used as the excitation wavelength, and the excitation laser power was  $1.3 \mu\text{W}$  to avoid heating, damaging, and nonlinear optical effects. The laser spot was around  $2 \mu\text{m}$ . PL mapping of  $\text{MoS}_2$ -IBCD in Figure 3 was obtained in the  $10 \times 10 \mu\text{m}^2$  region on the  $\text{MoS}_2$  monolayer. One scan took 2 s for a specific point, and the scan step size was  $1 \mu\text{m}$ . PL mapping of  $\text{MoS}_2$ -IBCD in Figure 4 was obtained in the  $1 \times 1 \mu\text{m}^2$  region on the  $\text{MoS}_2$  monolayer. Raman mapping of  $\text{MoS}_2$ -IBCD in Figure 4 was obtained in the  $1 \times 1 \mu\text{m}^2$  region on the  $\text{MoS}_2$  monolayer. One scan took 5 s for a specific point, and the scan step size was  $0.1 \mu\text{m}$ . Low temperature photoluminescence was carried out in a continuous flow He cryostat. The signal was collected and analyzed using a single spectrometer and a nitrogen-cooled charge-coupled device. To eliminate as many external factors besides temperature, we used same batch  $\text{MoS}_2$  monolayers grown under same parameters and

transferred it to the structure and non-structure regions using the polymer-assisted transfer method.

**Atomic Force Microscopy (AFM).** NT-MDT modular AFM is used for AFM measurement. The topographs are plotted with Gwyddion software.<sup>92</sup>

**Numerical Simulations.** Numerical simulations were conducted by the finite-difference time-domain (FDTD) method with determined graphical structure parameters. First, select an incident laser wavelength of 680 nm (the wavelength position corresponding to the MoS<sub>2</sub> monolayers PL peak at room temperature) on an 80 nm period of ideal blazed grating lines as the simplified IBCD structure for near field simulation to illustrate the electric field distribution of SPP modes. Representative structure parameters such as period, height, and blazed angle are from AFM topographs. Afterward, take representative periods of 80, 140, and 320 nm into transmittance simulation. TM polarization transmittance within the 250–900 nm wavelength range of incident laser in three periodicity regions was simulated.

## ■ ASSOCIATED CONTENT

### Supporting Information

The Supporting Information is available free of charge at <https://pubs.acs.org/doi/10.1021/acsnm.0c02386>.

AFM topographs of the IBCD structure sample at distances from the iron target of 10, 20, and 30 nm before and after 10 nm gold coating; MoS<sub>2</sub> monolayer images from the optical characterization platform under a 100× objective lens on regions with periods of (a) 80 nm, (b) 140 nm, and (c) 320 nm and (d) a flat region; measured transmittance curves of IBCD nanostructures at 80, 140, and 320 nm periodicity regions after 10 nm gold coating (PDF)

## ■ AUTHOR INFORMATION

### Corresponding Authors

**Sefaattin Tongay** – Materials Science and Engineering, School for Engineering of Matter, Transport and Energy, Arizona State University, Tempe, Arizona 85287, United States;

orcid.org/0000-0001-8294-984X;

Email: [Sefaattin.tongay@asu.edu](mailto:Sefaattin.tongay@asu.edu)

**Ying Liu** – National Synchrotron Radiation Laboratory, University of Science and Technology of China, Hefei 230029, P. R. China; orcid.org/0000-0001-8768-3155; Email: [liuychch@ustc.edu.cn](mailto:liuychch@ustc.edu.cn)

### Authors

**Yuheng Chen** – National Synchrotron Radiation Laboratory, University of Science and Technology of China, Hefei 230029, P. R. China

**Han Li** – Materials Science and Engineering, School for Engineering of Matter, Transport and Energy, Arizona State University, Tempe, Arizona 85287, United States

**Mark Blei** – Materials Science and Engineering, School for Engineering of Matter, Transport and Energy, Arizona State University, Tempe, Arizona 85287, United States

**Maoqi Cai** – National Synchrotron Radiation Laboratory, University of Science and Technology of China, Hefei 230029, P. R. China

**Haofeng Zang** – Department of Optics and Optical Engineering, University of Science and Technology of China, Hefei 230026, P. R. China

**Yonghua Lu** – Department of Optics and Optical Engineering, University of Science and Technology of China, Hefei 230026, P. R. China; orcid.org/0000-0003-1049-8474

Complete contact information is available at: <https://pubs.acs.org/doi/10.1021/acsnm.0c02386>

## Author Contributions

All authors have given approval to the final version of the manuscript.

## Notes

The authors declare no competing financial interest.

## ■ ACKNOWLEDGMENTS

This work was supported by the National Natural Science Foundation of China (grant no. 11675169). S.T. acknowledges support from NSF DMR 1552220, DMR 1955889, DMR 1904716, and NSF CMMI 1933214.

## ■ REFERENCES

- (1) Tsai, M.-L.; Su, S.-H.; Chang, J.-K.; Tsai, D.-S.; Chen, C.-H.; Wu, C.-I.; Li, L.-J.; Chen, L.-J.; He, J.-H. Monolayer MoS<sub>2</sub> Heterojunction Solar Cells. *ACS Nano* **2014**, *8*, 8317–8322.
- (2) Quy, V. H. V.; Vijayakumar, E.; Ho, P.; Park, J.-H.; Rajesh, J. A.; Kwon, J.; Chae, J.; Kim, J.-H.; Kang, S.-H.; Ahn, K.-S. Electrodeposited MoS<sub>2</sub> as electrocatalytic counter electrode for quantum dot- and dye-sensitized solar cells. *Electrochim. Acta* **2018**, *260*, 716–725.
- (3) Krishnan, U.; Kaur, M.; Singh, K.; Kaur, G.; Singh, P.; Kumar, M.; Kumar, A. MoS<sub>2</sub>/Ag nanocomposites for electrochemical sensing and photocatalytic degradation of textile pollutant. *J. Mater. Sci.: Mater. Med.* **2019**, *30*, 3711–3721.
- (4) Liu, X.; Hersam, M. C. 2D materials for quantum information science. *Nat. Rev. Mater.* **2019**, *4*, 669–684.
- (5) Qian, X.; Liu, J.; Fu, L.; Li, J. Quantum spin Hall effect in two-dimensional transition metal dichalcogenides. *Science* **2014**, *346*, 1344–1347.
- (6) Kalantar-zadeh, K.; Ou, J. Z.; Daeneke, T.; Strano, M. S.; Pumera, M.; Gras, S. L. Two-Dimensional Transition Metal Dichalcogenides in Biosystems. *Adv. Funct. Mater.* **2015**, *25*, 5086–5099.
- (7) Wen, X.; Gong, Z.; Li, D. Nonlinear optics of two-dimensional transition metal dichalcogenides. *InfoMat* **2019**, *1*, 317–337.
- (8) Krishnan, U.; Kaur, M.; Singh, K.; Kumar, M.; Kumar, A. A synoptic review of MoS<sub>2</sub>: Synthesis to applications. *Superlattices Microstruct.* **2019**, *128*, 274–297.
- (9) Pumera, M.; Loo, A. H. Layered transition-metal dichalcogenides (MoS<sub>2</sub> and WS<sub>2</sub>) for sensing and biosensing. *TrAC, Trends Anal. Chem.* **2014**, *61*, 49–53.
- (10) Zhang, Y.; Chang, T.-R.; Zhou, B.; Cui, Y.-T.; Yan, H.; Liu, Z.; Schmitt, F.; Lee, J.; Moore, R.; Chen, Y.; Lin, H.; Jeng, H.-T.; Mo, S.-K.; Hussain, Z.; Bansil, A.; Shen, Z.-X. Direct observation of the transition from indirect to direct bandgap in atomically thin epitaxial MoSe<sub>2</sub>. *Nat. Nanotechnol.* **2014**, *9*, 111–115.
- (11) He, K.; Kumar, N.; Zhao, L.; Wang, Z.; Mak, K. F.; Zhao, H.; Shan, J. Tightly bound excitons in monolayer WSe<sub>2</sub>. *Phys. Rev. Lett.* **2014**, *113*, 026803.
- (12) Kormányos, A.; Zólyomi, V.; Drummond, N. D.; Rakyta, P.; Burkard, G.; Fal'ko, V. I. Monolayer MoS<sub>2</sub>: Trigonal warping, the  $\Gamma$  valley, and spin-orbit coupling effects. *Phys. Rev. B* **2013**, *88*, 045416.
- (13) Yagmurcukardes, M.; Qin, Y.; Ozen, S.; Sayyad, M.; Peeters, F. M.; Tongay, S.; Sahin, H. Quantum properties and applications of 2D Janus crystals and their superlattices. *Appl. Phys. Rev.* **2020**, *7*, 011311.
- (14) Han, M. Y.; Özyilmaz, B.; Zhang, Y.; Kim, P. Energy band-gap engineering of graphene nanoribbons. *Phys. Rev. Lett.* **2007**, *98*, 206805.
- (15) Ni, Z. H.; Yu, T.; Lu, Y. H.; Wang, Y. Y.; Feng, Y. P.; Shen, Z. X. Uniaxial Strain on Graphene: Raman Spectroscopy Study and Band-Gap Opening. *ACS Nano* **2008**, *2*, 2301–2305.
- (16) Bai, J.; Zhong, X.; Jiang, S.; Huang, Y.; Duan, X. Graphene nanomesh. *Nat. Nanotechnol.* **2010**, *5*, 190–194.

- (17) Pan, H.; Zhang, Y.-W. Edge-dependent structural, electronic and magnetic properties of MoS<sub>2</sub> nanoribbons. *J. Mater. Chem.* **2012**, *22*, 7280–7290.
- (18) Wu, J. B.; Zhao, H.; Li, Y.; Ohlberg, D.; Shi, W.; Wu, W.; Wang, H.; Tan, P. H. Monolayer Molybdenum Disulfide Nanoribbons with High Optical Anisotropy. *Adv. Opt. Mater.* **2016**, *4*, 756–762.
- (19) Quereda, J.; San-Jose, P.; Parente, V.; Vaquero-Garzon, L.; Molina-Mendoza, A. J.; Agraït, N.; Rubio-Bollinger, G.; Guinea, F.; Roldán, R.; Castellanos-Gomez, A. Strong Modulation of Optical Properties in Black Phosphorus through Strain-Engineered Rippling. *Nano Lett.* **2016**, *16*, 2931–2937.
- (20) Kou, L.; Tang, C.; Zhang, Y.; Heine, T.; Chen, C.; Frauenheim, T. Tuning Magnetism and Electronic Phase Transitions by Strain and Electric Field in Zigzag MoS<sub>2</sub> Nanoribbons. *J. Phys. Chem. Lett.* **2012**, *3*, 2934–2941.
- (21) Mak, K. F.; Lee, C.; Hone, J.; Shan, J.; Heinz, T. F. Atomically thin MoS<sub>2</sub>: a new direct-gap semiconductor. *Phys. Rev. Lett.* **2010**, *105*, 136805.
- (22) Splendiani, A.; Sun, L.; Zhang, Y.; Li, T.; Kim, J.; Chim, C. Y.; Galli, G.; Wang, F. Emerging photoluminescence in monolayer MoS<sub>2</sub>. *Nano Lett.* **2010**, *10*, 1271–1275.
- (23) Wang, Q. H.; Kalantar-Zadeh, K.; Kis, A.; Coleman, J. N.; Strano, M. S. Electronics and optoelectronics of two-dimensional transition metal dichalcogenides. *Nat. Nanotechnol.* **2012**, *7*, 699–712.
- (24) Cao, T.; Wang, G.; Han, W.; Ye, H.; Zhu, C.; Shi, J.; Niu, Q.; Tan, P.; Wang, E.; Liu, B.; Feng, J. Valley-selective circular dichroism of monolayer molybdenum disulfide. *Nat. Commun.* **2012**, *3*, 887.
- (25) Xiao, D.; Liu, G. B.; Feng, W.; Xu, X.; Yao, W. Coupled spin and valley physics in monolayers of MoS<sub>2</sub> and other group-VI dichalcogenides. *Phys. Rev. Lett.* **2012**, *108*, 196802.
- (26) Zeng, H.; Dai, J.; Yao, W.; Xiao, D.; Cui, X. Valley polarization in MoS<sub>2</sub> monolayers by optical pumping. *Nat. Nanotechnol.* **2012**, *7*, 490–493.
- (27) Wu, S.; Buckley, S.; Schaibley, J. R.; Feng, L.; Yan, J.; Mandrus, D. G.; Hatami, F.; Yao, W.; Vučković, J.; Majumdar, A.; Xu, X. Monolayer semiconductor nanocavity lasers with ultralow thresholds. *Nature* **2015**, *520*, 69–72.
- (28) Ye, Y.; Wong, Z. J.; Lu, X.; Ni, X.; Zhu, H.; Chen, X.; Wang, Y.; Zhang, X. Monolayer excitonic laser. *Nat. Photonics* **2015**, *9*, 733–737.
- (29) Palacios-Berraquero, C.; Barbone, M.; Kara, D. M.; Chen, X.; Goykhman, I.; Yoon, D.; Ott, A. K.; Beitner, J.; Watanabe, K.; Taniguchi, T.; Ferrari, A. C.; Atatüre, M. Atomically thin quantum light-emitting diodes. *Nat. Commun.* **2016**, *7*, 12978.
- (30) Zhang, Y. J.; Oka, T.; Suzuki, R.; Ye, J. T.; Iwasa, Y. Electrically Switchable Chiral Light-Emitting Transistor. *Science* **2014**, *344*, 725–728.
- (31) Camellini, A.; Mennucci, C.; Cinquanta, E.; Martella, C.; Mazzanti, A.; Lamperti, A.; Molle, A.; de Mongeot, F. B.; Della Valle, G.; Zavelani-Rossi, M. Ultrafast Anisotropic Exciton Dynamics in Nanopatterned MoS<sub>2</sub> Sheets. *ACS Photonics* **2018**, *5*, 3363–3371.
- (32) Scalise, E.; Houssa, M.; Pourtois, G.; Afanas'ev, V.; Stesmans, A. Strain-induced semiconductor to metal transition in the two-dimensional honeycomb structure of MoS<sub>2</sub>. *Nano Res.* **2011**, *5*, 43–48.
- (33) Ellis, J. K.; Lucero, M. J.; Scuseria, G. E. The indirect to direct band gap transition in multilayered MoS<sub>2</sub> as predicted by screened hybrid density functional theory. *Appl. Phys. Lett.* **2011**, *99*, 261908.
- (34) Xu, Z.-Q.; Zhang, Y.; Wang, Z.; Shen, Y.; Huang, W.; Xia, X.; Yu, W.; Xue, Y.; Sun, L.; Zheng, C.; Lu, Y.; Liao, L.; Bao, Q. Atomically thin lateral p-n junction photodetector with large effective detection area. *2D Mater.* **2016**, *3*, 041001.
- (35) Wu, S.; Buckley, S.; Jones, A. M.; Ross, J. S.; Ghimire, N. J.; Yan, J.; Mandrus, D. G.; Yao, W.; Hatami, F.; Vučković, J.; Majumdar, A.; Xu, X. Control of two-dimensional excitonic light emission via photonic crystal. *2D Mater.* **2014**, *1*, 011001.
- (36) Chen, H.; Nanz, S.; Abass, A.; Yan, J.; Gao, T.; Choi, D.-Y.; Kivshar, Y. S.; Rockstuhl, C.; Neshev, D. N. Enhanced Directional Emission from Monolayer WSe<sub>2</sub> Integrated onto a Multiresonant Silicon-Based Photonic Structure. *ACS Photonics* **2017**, *4*, 3031–3038.
- (37) Galfsky, T.; Sun, Z.; Conside, C. R.; Chou, C.-T.; Ko, W. C.; Lee, Y.-H.; Narimanov, E. E.; Menon, V. M. Broadband Enhancement of Spontaneous Emission in Two-Dimensional Semiconductors Using Photonic Hypercrystals. *Nano Lett.* **2016**, *16*, 4940–4945.
- (38) Butun, S.; Tongay, S.; Aydin, K. Enhanced light emission from large-area monolayer MoS<sub>2</sub> using plasmonic nanodisc arrays. *Nano Lett.* **2015**, *15*, 2700–2704.
- (39) Chen, H.; Yang, J.; Rusak, E.; Straubel, J.; Guo, R.; Myint, Y. W.; Pei, J.; Decker, M.; Staude, I.; Rockstuhl, C.; Lu, Y.; Kivshar, Y. S.; Neshev, D. Manipulation of photoluminescence of two-dimensional MoSe<sub>2</sub> by gold nanoantennas. *Sci. Rep.* **2016**, *6*, 22296.
- (40) Wang, J.-F.; Zhou, H.-L.; Xiong, X.; Li, Q.; Cheng, Z.-D.; Liu, Z.-H.; Yan, F.-F.; Lin, S.-R.; Xu, J.-S.; Wang, G.-Z.; Wu, L.; Li, C.-F.; Guo, G.-C. Cavity-enhanced energy transfer between nano-emitters and monolayer graphene. *Carbon* **2020**, *161*, 794–799.
- (41) Novotny, L.; van Hulst, N. Antennas for light. *Nat. Photonics* **2011**, *5*, 83–90.
- (42) Schuller, J. A.; Barnard, E. S.; Cai, W.; Jun, Y. C.; White, J. S.; Brongersma, M. L. Plasmonics for extreme light concentration and manipulation. *Nat. Mater.* **2010**, *9*, 193–204.
- (43) Kinkhabwala, A.; Yu, Z.; Fan, S.; Avlasevich, Y.; Müllen, K.; Moerner, W. E. Large single-molecule fluorescence enhancements produced by a bowtie nanoantenna. *Nat. Photonics* **2009**, *3*, 654–657.
- (44) Li, L.; Chen, E. H.; Zheng, J.; Mouradian, S. L.; Dolde, F.; Schröder, T.; Karaveli, S.; Markham, M. L.; Twitchen, D. J.; Englund, D. Efficient photon collection from a nitrogen vacancy center in a circular bullseye grating. *Nano Lett.* **2015**, *15*, 1493–1497.
- (45) Kuo, S.-J.; Tsai, P.-C.; Lee, Y.-C.; Chang, S.-W.; Sotoma, S.; Fang, C.-Y.; Chang, H.-C.; Chen, H.-L. Manipulating the distribution of electric field intensity to effectively enhance the spatial and spectral fluorescence intensity of fluorescent nanodiamonds. *Nanoscale* **2018**, *10*, 17576–17584.
- (46) Lee, Y.-C.; Tseng, Y.-C.; Chen, H.-L. Single type of nanocavity structure enhances light outcouplings from various two-dimensional materials by over 100-fold. *ACS Photonics* **2017**, *4*, 93–105.
- (47) Willets, K. A.; Van Duyne, R. P. Localized surface plasmon resonance spectroscopy and sensing. *Annu. Rev. Phys. Chem.* **2007**, *58*, 267–297.
- (48) Kochuveedu, S. T.; Kim, D. H. Surface plasmon resonance mediated photoluminescence properties of nanostructured multi-component fluorophore systems. *Nanoscale* **2014**, *6*, 4966–4984.
- (49) Mukherjee, B.; Kaushik, N.; Tripathi, R. P. N.; Joseph, A. M.; Mohapatra, P. K.; Dhar, S.; Singh, B. P.; Kumar, G. V. P.; Simsek, E.; Lodha, S. Exciton Emission Intensity Modulation of Monolayer MoS<sub>2</sub> via Au Plasmon Coupling. *Sci. Rep.* **2017**, *7*, 41175.
- (50) Han, C.; Ye, J. Polarized resonant emission of monolayer WS<sub>2</sub> coupled with plasmonic sawtooth nanoslit array. *Nat. Commun.* **2020**, *11*, 713.
- (51) Kang, Y.; Li, B.; Fang, Z. Radiative energy transfer from MoS<sub>2</sub> excitons to surface plasmons. *J. Opt. A: Pure Appl. Opt.* **2017**, *19*, 124009.
- (52) Cho, C.-H.; Aspetti, C. O.; Park, J.; Agarwal, R. Silicon coupled with plasmon nanocavity generates bright visible hot-luminescence. *Nat. Photonics* **2013**, *7*, 285–289.
- (53) Baffou, G.; Quidant, R. Thermo-plasmonics: using metallic nanostructures as nano-sources of heat. *Laser Photonics Rev.* **2013**, *7*, 171–187.
- (54) Singha, S. S.; Nandi, D.; Bhattacharya, T. S.; Mondal, P. K.; Singha, A. Photoluminescence modulation due to conversion of trions to excitons and plasmon interaction in MoS<sub>2</sub>-metal NPs hybrid structures. *J. Alloys Compd.* **2017**, *723*, 722–728.
- (55) Liu, W.; Lee, B.; Naylor, C. H.; Ee, H.-S.; Park, J.; Johnson, A. T. C.; Agarwal, R. Strong Exciton-Plasmon Coupling in MoS<sub>2</sub> Coupled with Plasmonic Lattice. *Nano Lett.* **2016**, *16*, 1262–1269.
- (56) Kang, Y.; Najmaei, S.; Liu, Z.; Bao, Y.; Wang, Y.; Zhu, X.; Halas, N. J.; Nordlander, P.; Ajayan, P. M.; Lou, J.; Fang, Z.

Plasmonic hot electron induced structural phase transition in a MoS<sub>2</sub> monolayer. *Adv. Mater.* **2014**, *26*, 6467–6471.

(57) Körner, M.; Röder, F.; Lenz, K.; Fritzsche, M.; Lindner, J.; Lichte, H.; Fassbender, J. Quantitative imaging of the magnetic configuration of modulated nanostructures by electron holography. *Small* **2014**, *10*, S161–S169.

(58) Savvides, N. Surface microroughness of ion-beam etched optical surfaces. *J. Appl. Phys.* **2005**, *97*, 053517.

(59) Aparimita, A.; Naik, R.; Sahoo, S.; Sripan, C.; Ganesan, R. Influence of low energy Ag ion irradiation for formation of Bi<sub>2</sub>Se<sub>3</sub> phase from Bi/GeSe<sub>2</sub> heterostructure thin films. *Appl. Phys. A: Mater. Sci. Process.* **2020**, *126*, 203.

(60) Harrison, M. P.; Bradley, R. M. Fabrication of high quality multilayer blazed gratings using ion beam assisted deposition. *J. Appl. Phys.* **2017**, *121*, 225304.

(61) Toma, A.; Chiappe, D.; Massabò, D.; Boragno, C.; Buatier de Mongeot, F. Self-organized metal nanowire arrays with tunable optical anisotropy. *Appl. Phys. Lett.* **2008**, *93*, 163104.

(62) Zabolian, H.; Fallah, H.; Rahimi, G.; Khashei, H.; Isfahan, S. P. Effect of anode surface treatment by oblique ion bombardment method on organic light-emitting diodes performance. *Surf. Interfaces* **2019**, *17*, 100390.

(63) Saerbeck, T.; Huckfeldt, H.; Toperverg, B. P.; Ehresmann, A. Magnetic Structure of Ion-Beam Imprinted Stripe Domains Determined by Neutron Scattering. *Nanomaterials* **2020**, *10*, 752.

(64) Bradley, R. M. Producing ripple topographies by ion bombardment with codeposition of impurities: A curvature-dependent sputter yield is not required. *Phys. Rev. B* **2012**, *85*, 115419.

(65) Ozaydin, G.; Ludwig, K. F.; Zhou, H.; Headrick, R. L. Effects of Mo seeding on the formation of Si nanodots during low-energy ion bombardment. *J. Vac. Sci. Technol., B* **2008**, *26*, 551–557.

(66) Macko, S.; Frost, F.; Ziberi, B.; Förster, D. F.; Michely, T. Is keV ion-induced pattern formation on Si(001) caused by metal impurities? *Nanotechnology* **2010**, *21*, 085301.

(67) Engler, M.; Frost, F.; Müller, S.; Macko, S.; Will, M.; Feder, R.; Spemann, D.; Hübner, R.; Facsko, S.; Michely, T. Silicide induced ion beam patterning of Si(001). *Nanotechnology* **2014**, *25*, 115303.

(68) Hofsäuss, H.; Zhang, K. Surfactant sputtering. *Appl. Phys. A: Mater. Sci. Process.* **2008**, *92*, 517–524.

(69) Liu, Y.; Hirsch, D.; Fechner, R.; Hong, Y.; Fu, S.; Frost, F.; Rauschenbach, B. Nanostructures on fused silica surfaces produced by ion beam sputtering with Al co-deposition. *Appl. Phys. A* **2017**, *124*, 73.

(70) Chen, D.; Yang, G.; Li, J.; Hirsch, D.; Liu, Y.; Frost, F.; Hong, Y. Terrace morphology on fused silica surfaces by Ar<sup>+</sup> ion bombardment with Mo co-deposition. *Appl. Phys. Lett.* **2018**, *113*, 033102.

(71) Castellanos-Gomez, A.; Buscema, M.; Molenaar, R.; Singh, V.; Janssen, L.; van der Zant, H. S. J.; Steele, G. A. Deterministic transfer of two-dimensional materials by all-dry viscoelastic stamping. *2D Mater.* **2014**, *1*, 011002.

(72) Martella, C.; Mennucci, C.; Cinquanta, E.; Lamperti, A.; Cappelluti, E.; Buatier de Mongeot, F.; Molle, A. Anisotropic MoS<sub>2</sub> Nanosheets Grown on Self-Organized Nanopatterned Substrates. *Adv. Mater.* **2017**, *29*, 1605785.

(73) Catalán-Gómez, S.; Briones, M.; Cortijo-Campos, S.; García-Mendiola, T.; de Andrés, A.; Garg, S.; Kung, P.; Lorenzo, E.; Pau, J. L.; Redondo-Cubero, A. Breast cancer biomarker detection through the photoluminescence of epitaxial monolayer MoS<sub>2</sub> flakes. *Sci. Rep.* **2020**, *10*, 16039.

(74) Li, H.; Zhang, Q.; Yap, C. C. R.; Tay, B. K.; Edwin, T. H. T.; Olivier, A.; Baillargeat, D. From Bulk to Monolayer MoS<sub>2</sub>: Evolution of Raman Scattering. *Adv. Funct. Mater.* **2012**, *22*, 1385–1390.

(75) Lee, C.; Yan, H.; Brus, L. E.; Heinz, T. F.; Hone, J.; Ryu, S. Anomalous Lattice Vibrations of Single and Few-Layer MoS<sub>2</sub>. *ACS Nano* **2010**, *4*, 2695–2700.

(76) Joo, P.; Jo, K.; Ahn, G.; Voiry, D.; Jeong, H. Y.; Ryu, S.; Chhowalla, M.; Kim, B.-S. Functional Polyelectrolyte Nanospaced

MoS<sub>2</sub> Multilayers for Enhanced Photoluminescence. *Nano Lett.* **2014**, *14*, 6456–6462.

(77) Hu, Y.; Zhang, F.; Titze, M.; Deng, B.; Li, H.; Cheng, G. J. Straining effects in MoS<sub>2</sub> monolayer on nanostructured substrates: temperature-dependent photoluminescence and exciton dynamics. *Nanoscale* **2018**, *10*, 5717–5724.

(78) Wang, Y.; Cong, C.; Qiu, C.; Yu, T. Raman Spectroscopy Study of Lattice Vibration and Crystallographic Orientation of Monolayer MoS<sub>2</sub> under Uniaxial Strain. *Small* **2013**, *9*, 2857–2861.

(79) Rice, C.; Young, R. J.; Zan, R.; Bangert, U.; Wolverson, D.; Georgiou, T.; Jalil, R.; Novoselov, K. S. Raman-scattering measurements and first-principles calculations of strain-induced phonon shifts in monolayer MoS<sub>2</sub>. *Phys. Rev. B* **2013**, *87*, 081307.

(80) Chang, C.-Y.; Lin, H.-T.; Lai, M.-S.; Yu, C.-L.; Wu, C.-R.; Chou, H.-C.; Lin, S.-Y.; Chen, C.; Shih, M.-H. Large-Area and Strain-Reduced Two-Dimensional Molybdenum Disulfide Monolayer Emitters on a Three-Dimensional Substrate. *ACS Appl. Mater. Interfaces* **2019**, *11*, 26243–26249.

(81) Polyanskiy, M. *Refractive index database*; [refractiveindex.info](https://refractiveindex.info). <https://refractiveindex.info/>, 2020.

(82) McPeak, K. M.; Jayanti, S. V.; Kress, S. J. P.; Meyer, S.; Iotti, S.; Rossinelli, A.; Norris, D. J. Plasmonic films can easily be better: Rules and recipes. *ACS Photonics* **2015**, *2*, 326–333.

(83) Malitson, I. H. Interspecimen comparison of the refractive index of fused silica. *J. Opt. Soc. Am.* **1965**, *55*, 1205–1208.

(84) Ebbesen, T. W.; Lezec, H. J.; Ghaemi, H. F.; Thio, T.; Wolff, P. A. Extraordinary optical transmission through sub-wavelength hole arrays. *Nature* **1998**, *391*, 667–669.

(85) Ushkov, A. A.; Shcherbakov, A. A.; Verrier, I.; Kampfe, T.; Jourlin, Y. Systematic study of resonant transmission effects in visible band using variable depth gratings. *Sci. Rep.* **2019**, *9*, 14890.

(86) Toma, A.; Chiappe, D.; Boragno, C.; Buatier de Mongeot, F. Self-organized ion-beam synthesis of nanowires with broadband plasmonic functionality. *Phys. Rev. B: Condens. Matter Mater. Phys.* **2010**, *81*, 165436.

(87) Ranjan, M.; Facsko, S.; Fritzsche, M.; Mukherjee, S. Plasmon resonance tuning in Ag nanoparticles arrays grown on ripple patterned templates. *Microelectron. Eng.* **2013**, *102*, 44–47.

(88) Zhao, L.; Kelly, K. L.; Schatz, G. C. The Extinction Spectra of Silver Nanoparticle Arrays: Influence of Array Structure on Plasmon Resonance Wavelength and Width. *J. Phys. Chem. B* **2003**, *107*, 7343–7350.

(89) Resano-Garcia, A.; Battie, Y.; En Naciri, A.; Akil, S.; Chaoui, N. Experimental and theoretical determination of the plasmonic responses and shape distribution of colloidal metallic nanoparticles. *J. Chem. Phys.* **2015**, *142*, 134108.

(90) Sevik, C. Assessment on lattice thermal properties of two-dimensional honeycomb structures: Graphene, h-BN, h-MoS<sub>2</sub>, and h-MoSe<sub>2</sub>. *Phys. Rev. B* **2014**, *89*, 035422.

(91) Huang, L. F.; Gong, P. L.; Zeng, Z. Correlation between structure, phonon spectra, thermal expansion, and thermomechanics of single-layer MoS<sub>2</sub>. *Phys. Rev. B* **2014**, *90*, 045409.

(92) Nečas, D.; Klapetek, P. *Gwyddion-Free SPM (AFM, SNOM/NSOM, STM, MFM, ...)* data analysis software; <http://gwyddion.net/>, 01, 2019.